JOC The Journal of Organic Chemistry

Article

pubs.acs.org/joc

Competing Mechanisms, Substituent Effects, and Regioselectivities of Nickel-Catalyzed [2 + 2 + 2] Cycloaddition between Carboryne and Alkynes: A DFT Study

Wei-Hua Mu,*[,†] Shu-Ya Xia,[†] Ji-Xiang Li,[†] De-Cai Fang,[‡] Gang Wei,[§] and Gregory A Chass*[,∥]

[†]Faculty of Chemistry and Chemical Engineering, Yunnan Normal University, Kunming 650092, Yunnan, China

[‡]Key Laboratory of Theoretical and Computational Photochemistry, Ministry of Education, College of Chemistry, Beijing Normal University, Beijing 100875, China

[§]CSIRO Manufacturing Flagship, Bradfield Road, West Lindfield, P.O. Box 218, Lindfield, NSW 2070, Australia

[∥]School of Biological and Chemical Sciences, Queen Mary University of London, London E1 4NS, U.K.

Supporting Information

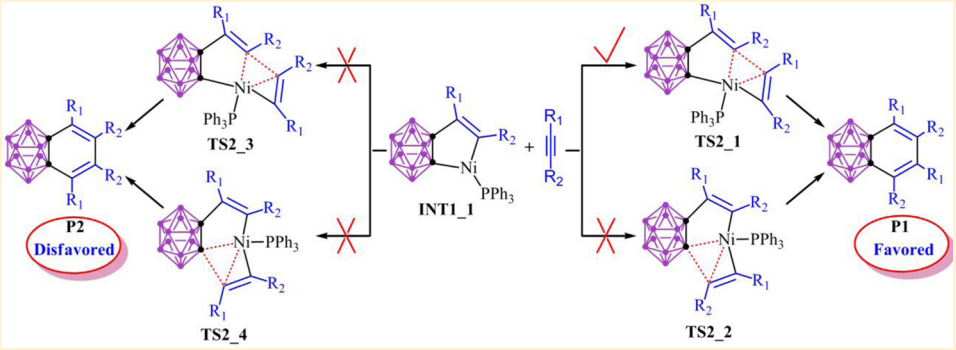

ABSTRACT: Competing reaction mechanisms, substituent effects, and regioselectivities of $Ni(PPh_3)_2$-catalyzed [2 + 2 + 2] carboryne−alkyne cycloadditions were characterized by density functional theory using the real chemical systems and solvent effects considered. A putative mechanism involving the following steps was characterized: (1) exothermic carboryne−catalyst complexation and nucleophilic attack by the first alkyne; (2) insertion of the second alkyne, the rate-determining step (RDS) in all four reactions studied; (3) isomerization of reactant-bound complexes; and (4) product elimination and catalyst regeneration. The RDS in three reactions is mediated by free energy barriers of 27.2, 31.1, and 36.6 kcal·mol^{-1}, representative of the corresponding experimental yields of 67, 54, and 33%, respectively. A fourth reaction with 0% experimental yield showed representative RDS free energy barriers of 60.4 kcal·mol^{-1}, which are difficult to surmount even at 90 °C. Alternative pathways leading to differing isomers were similarly characterized and successfully reproduced experimentally determined product regioselectivities. Kinetic data derived from free energy barriers are in quantitative agreement (< ± 0.75−3.0 kcal·mol^{-1}) of the experimental times, affirming the theoretical results as representative of the real chemical transformations. Complementary determinations show the use of truncated models ($Ni(PMe_3)_2$, $Ni(PH_3)_2$) causes the RDS to vary from step 2 (alkyne insertion) to step 1 (alkyne attack), highlighting the need to employ real chemical systems in modeling these reactions.

1. INTRODUCTION

Construction of carbon−carbon bonds through transition-metal-catalyzed cross-coupling reactions is now a highly efficient and universal route in the synthetic toolbox, garnering significant research activity.[1] Recently, Ni-catalyzed [2 + 2 + 2] cross-coupling cyclization reactions have been shown to be effective paths to the construction of six-membered ring containing compounds of biological and physiologic significance.[2]

Ni-catalyzed [2 + 2 + 2] cross-coupling cyclizations of carborynes and alkynes have been established as a viable route to constructing highly substituted benzocarboranes (Scheme 1).[3] The idea arose from detailed synthetic explorations with benzyne,[4] a dimensional relative of carboryne (1,2-dehydro-*o*-carborane).[5] These Ni-catalyzed reactions show good regioselectivities, and alkynes substituted with an electron-donating group (EDG) such as an ethyl moiety (Et) generated higher yields than those substituted with an electron-withdrawing group (EWG) such as phenyl (Ph). However, an alkyne substituted with a bulky EDG was found to be a poor reactant for benzocarborane formation (reaction **d** in Scheme 1).

Putative mechanisms for benzocarborane formation are buoyed by experimental works to expand the tolerance and

Received: June 27, 2015
Published: August 13, 2015

DOI: 10.1021/acs.joc.5b01464
J. Org. Chem. 2015, 80, 9108−9117

Scheme 1. Four Ni-Catalyzed [2 + 2 + 2] Carboryne–alkyne Cycloaddition Reactions Studied in This Work[a]

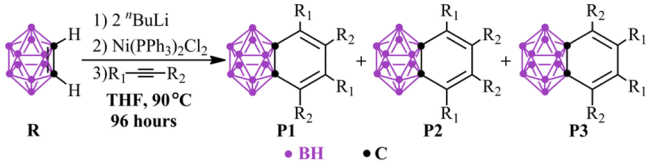

	R_1	R_2	Product	Yield(%)*
a	Et	Et	P1a	67(8)
b	Ph	Ph	P1b	33(0)
c	Me	Ph	P1c/P2c/P3c	54(0)/0/0
d	*t*Bu	*n*Bu	P1d/P2d/P3d	NR/NR/NR

*Yields in parentheses correspond to benzene derivatives.

[a]Boron and carbon atoms in the $B_{10}H_{10}C_2$ fragments are represented by purple and black dots, respectively, while H-atoms on borons are omitted for clarity.

adaptability of these Ni-catalyzed [2 + 2 + 2] cycloadditions to carborynes and unsaturated compounds, including alkenes and alkynes,[6] benzene derivatives,[7] anisoles,[8] ethers,[9] ferrocene,[10] and other unsaturated molecules.[11] Despite these synthetic successes, no complementary theoretical characterizations have yet been completed to quantitatively resolve the strong substituent effects and pronounced regioselectivities empirically demonstrated in this reaction.

Building on the pioneering efforts of Xie et al. using truncated models for [2 + 2 + 1]-type reactions,[12] we initiated a series of all-electron density functional theory (DFT) determinations on these Ni-catalyzed [2 + 2 + 2] transformations in THF solution with the objective of resolving the chemical bases for the observed regioselectivities.

2. RESULTS AND DISCUSSION

Preliminary determinations were completed with the IDSCRF-B3LYP method and the all-electron DGDZVP basis set at an experimental temperature of 363 K. Solvent effects were addressed using the implicit SCRF-PCM solvent method with THF as solvent and condensed-phase contributions of translational entropy, representative of the phase of the reaction (see the Computational Details).

Basis set superposition error (BSSE) was quantified for RDS barriers to ensure it did not compromise the trends uncovered. BSSE is a phenomenon arising from comparative evaluation of the relative energies of complexes, intermediates and transition states with respect to their separated components (i.e., ΔG_{rel} (catalyst + reactants) vs ΔG_{rel} (catalyst-reactants). BSSE was determined to be 5.7, 7.2, 6.3, and 6.7 kcal·mol^{-1} (Table S1), respectively, for the RDSs in reactions **a**–**d** (**TS2_1a**, **TS2_1b**, **TS2_1c**, and **TS2_2d**, respectively). Although noticeable, these BSSE contributions do not modulate the identity of the RDS, nor do they perturb reproduction of experimental yield ordering (a > c > b ≫ d), affirming BSSE as not being problematic to the determinations presented.

Additional determinations using the following DFT methods (all with the all-electron DGDZVP basis set) were trialed toward resolving the influence of computational method on observed result-trends: X3LYP, CAM-B3LYP, B3LYP+D3, and M062X. The results are presented in section 2.5.

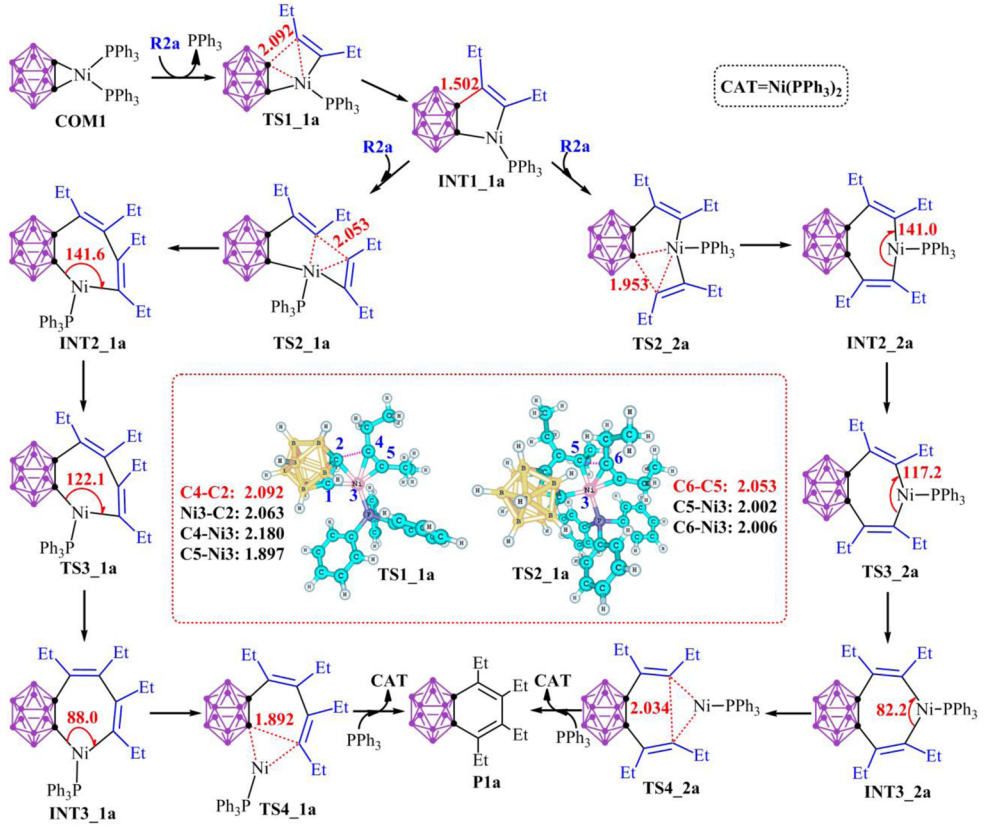

Figure 1. Reaction mechanism and key optimized structures for reaction **a**, computed at the IDSCRF-B3LYP/DGDZVP level in THF solvent at 363 K with selected bond lengths (Å) and bond angles (deg).

DOI: 10.1021/acs.joc.5b01464
J. Org. Chem. 2015, 80, 9108–9117

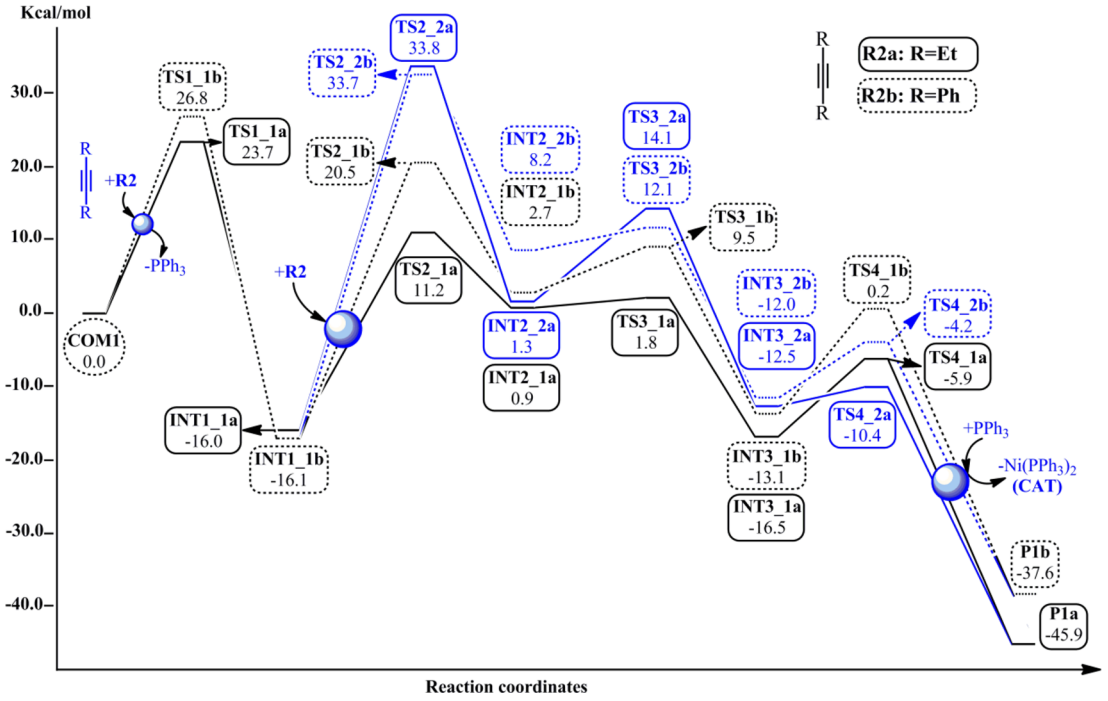

Figure 2. Reaction profiles and relative free energies (kcal·mol^{-1}) for reactions **a** and **b**, computed at the IDSCRF-B3LYP/DGDZVP level in THF solvent at 363 K. The two competing pathways in both reactions **a** and **b** are shown, labeled **1a**, **2a** (solid lines) and **1b**, **2b** (dashed lines), respectively. The predominant pathways are traced with black lines (**1a** and **1b**), while the minor pathways (**2a** and **2b**) are represented with blue lines.

2.1. Reaction Mechanism: Reaction a. Theoretical investigations of a putative Ni-catalyzed [2 + 2 + 2] carboryne−alkyne cycloaddition mechanism were initially carried out on the diethyl-substituted reactants (reaction **a**, Scheme 1) using the full reactants (i.e., no truncation of the real systems to simplified models) in implicit THF solvent. The mechanism and relevant geometric parameters are shown in Figure 1.

The first reaction step involves the $Ni(PPh_3)_2Cl_2$ catalyst easily forming a Ni−carboryne complex (**COM1**). This is assisted by $Li_2C_2B_{10}H_{10}$, which was experimentally prepared in situ through reaction of ^{n}BuLi with *o*-carborane.[3] Next, 3-hexyne (**R2a**) inserts into one of the two Ni−C bonds in **COM1** via **TS1_1a** with concurrent loss of a PPh_3 ligand from Ni, and a relative free energy (ΔG_{rel}) barrier of 23.7 kcal·mol^{-1} in THF at 363 K (**TS1_1a** in Figure 2).

This **TS1_1a** structure exothermically relaxes to form the five-membered intermediate **INT1_1a**. After this point, the mechanism bifurcates along two pathways labeled **1a** and **2a**, respectively, arising from two differing Ni−C insertion sites for the second equivalent of 3-hexyne (**R2a**). These routes are moderated by **TS2_1a** and **TS2_2a**, with ΔG_{rel} = 27.2 and 49.8 kcal·mol^{-1}, respectively, effectively making the **2a** pathway noncontributory to the final product. The proximity of the aryl groups in the PPh_3 ligand to the carborane allows for stabilizing interactions in the **TS2_1a** structure (quantified in section 2.5), yet are not possible for **TS2_2a**, contributing to the raised energetics. A much higher free energy barrier of **TS3_2a** (12.8 kcal·mol^{-1}, corresponding to **INT2_2a** → **INT3_2a** isomerization) than that of **TS3_1a** (0.9 kcal·mol^{-1}) further confirms the predomination of pathway **1a** at this step.

The fourth and final step involves formation of the product benzocarborane with concurrent regeneration of the catalyst via the **TS4** structures. Despite the **1a** pathway predominating, the final step in the minor **2a** path is in actuality 4.5 kcal·mol^{-1} more favorable in free energy (G_{rel} **TS4_1a** and **TS4_2a** = −5.9 and −10.4 kcal·mol^{-1}, respectively, relative to the starting materials), affirming the predictions made from empirical trends by Xie. Z et al.[3] Further, the relative activation barriers show similar trends, with the **2a** pathway having more easily activated transition structures (ΔG_{rel} **TS4_1a** and **TS4_2a** = 10.6 and 2.1 kcal·mol^{-1}, respectively). In summary, insertion of the second alkyne (**INT1_1a** → **TS2_1a** → **INT2_1a**) presents the highest free energy barrier, thus is the rate-determining step (RDS) in reaction **a** as well as within the **1a** pathway.

2.2. Substituent Effect. *2.2.1. Ph Substitution: Reaction b.* The free energy profile for reaction **b** (Figure 2) is similar to that of reaction **a**, with the initially shared reaction channel bifurcating upon addition of the second equivalent of alkyne (in this case, **R2b**). The second insertion is mediated by **TS2_1b** and **TS2_2b** (ΔG_{rel} = 36.6 and 49.8 kcal·mol^{-1}, respectively), making this step the RDS for both the **1b** and **2b** channels. The additional 13.2 kcal·mol^{-1} required for the **2b** channel (with respect to **1b**) renders it unfeasible, and thus, the generation of product **P1b** through this pathway negligible, in agreement with experimental predictions.[3] After facile **INT2** → **INT3** isomerization, similar to reaction **a**, the reaction proceeds with formation of product benzocarborane and concurrent regeneration of the catalyst via **TS4_1b** and **TS4_2b** (ΔG_{rel} = 13.3 and 7.8 kcal·mol^{-1}, respectively). This final barrier is relatively easy to surmount, with respect to the two preceding barriers. This substitution of the R group (Et, in **1a** profile) to Ph raises the RDS barrier by 9.4 kcal·mol^{-1}, mirroring the drop in experimental yields from **P1a** to **P1b** (67 vs 33%, Scheme 1), due to the sterics imposed by the bulkier group retarding the approach of the second alkyne.

DOI: 10.1021/acs.joc.5b01464
J. Org. Chem. 2015, 80, 9108−9117

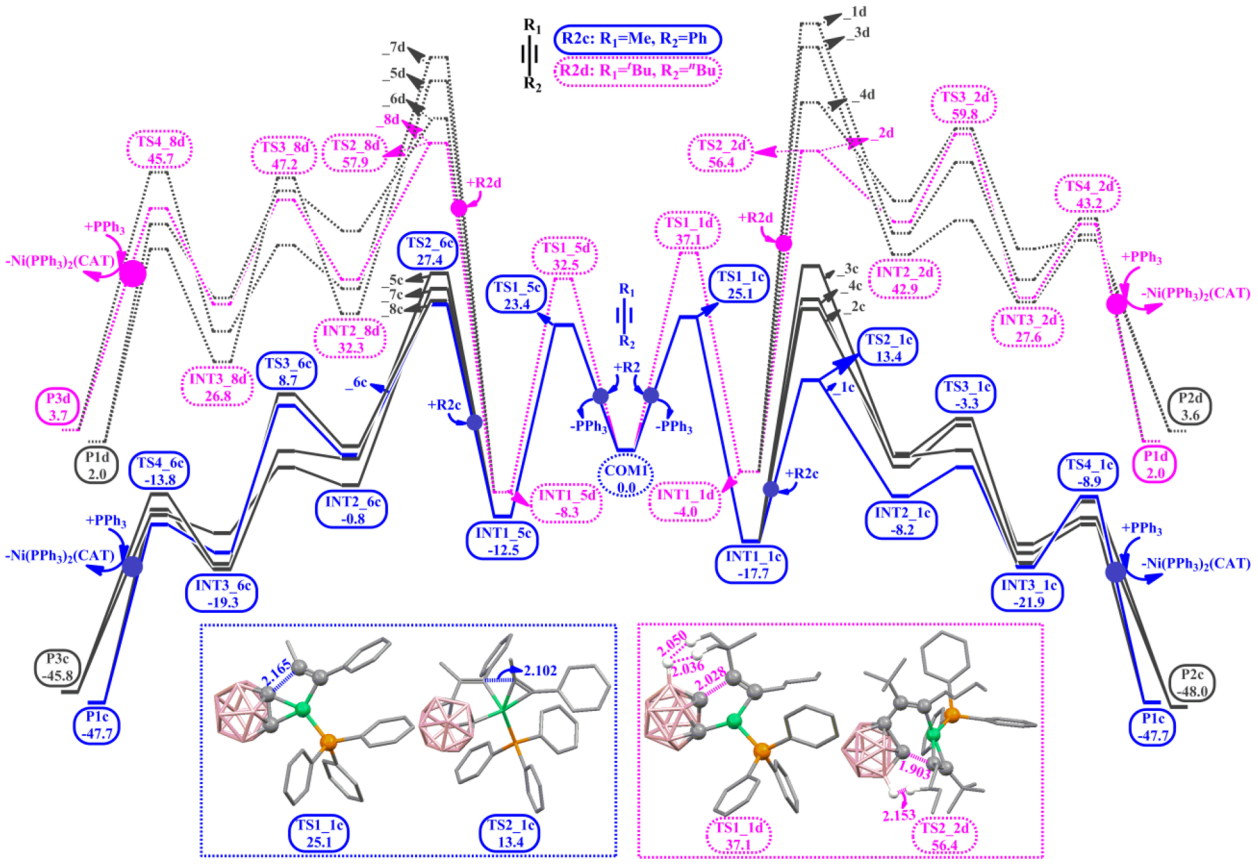

Figure 3. Reaction profiles and relative free energies (kcal·mol^{-1}) for reactions **c** and **d** (**COM1** + **R2c** → **P1c**/**P2c**/**P3c**, **COM1** + **R2d** → **P1d**/**P2d**/**P3d**), computed at the IDSCRF-B3LYP/DGDZVP level in THF solvent at 363 K.

2.2.2. Ph and Me Substitution: Reaction ***c****.* Substituent effects on alkyne regioselectivities, including unsymmetrical alkynes, were subsequently explored (reaction **c**, Scheme 1). Eight possible reaction channels leading to three differing benzocarborane products (**P1c**, **P2c**, and **P3c**) were located. ΔG_{rel} values for stationary points and first order TSs along the optimal reaction channel (**1c**) are provided in Figure 3; comparative profiles (**2c** to **8c**) are coplotted in Figure 3. Geometric structures and detailed reaction profiles along all pathways (**1c** to **8c**) are provided in Figure S1.

The initial step, insertion of the carboryne to the C−Ni bond, bifurcates the reaction profile along two differing pathways (starting at **COM1** in the center and branching left and right in Figure 3), mediated by **TS1_1c** (ΔG_{rel} = 25.1 kcal·mol^{-1}, for paths **1c**−**4c**) and **TS1_5c** (ΔG_{rel} = 23.4 kcal·mol^{-1}, for paths **5c**−**8c**). Overall, the pathway accessed via **TS1_1c** (right side of Figure 3) is the predominant one, despite having an initial free energy barrier 1.7 kcal·mol^{-1} higher than that of **TS1_5c** (left side of Figure 3), as all subsequent barriers have more favorable energetics along the remainder of the reaction profile. Specifically, the **1c** pathway has a free energy barrier of 31.1 kcal·mol^{-1} for the subsequent addition of the second equivalent of hexyne via **TS2_1c** and serves as the RDS for this pathway. This **TS2** event presents even higher barriers for all of the three other paths along this **TS1_1c** "right channel" (ΔG_{rel} = 44.7−52.6 kcal·mol^{-1}) and the four along the **TS1_5c** "left channel" (ΔG_{rel} = 39.9−46.2 kcal·mol^{-1}) and, thus, **TS2** the RDS for paths **2c**−**4c** and **5c**−**8c**.

In summary, the dominant pathway is **1c** in reaction **c**, as in reactions **a** and **b**, with the RDS once again being the insertion of the second equivalent of alkyne. The RDS of path **1c** is ∼3.9 kcal·mol^{-1} less favorable than **1a**, helping explain the experimental yields observed for **P1c** being reduced with respect to **P1a** (54 vs 67%, Scheme 1). Theory also shows products **P2c** and **P3c** to be blocked by energetically unfeasible barriers (**3c**/**4c** and **7c**/**8c**, respectively, Figure S1), again in agreement with experimental observations of negligible yields (0%, Scheme 1); further evidencing the theory as being representative.

2.2.3. Bulky Substituents: Reaction ***d****.* The use of bulky substituents such as ^{t}Bu and ^{n}Bu shuts the reaction down with no detectable yields of desired products under the experimental conditions employed (reaction **d**, Scheme 1). Toward explaining this termination of reactivity and the absence of desired products (**P1d**, **P2d**, and **P3d** in this case), the transformations using ^{t}Bu- and ^{n}Bu-substituted alkynes were characterized in the same manner as reactions **a**−**c**.

Overall, the results showed a resultant reaction profile with features similar to those of reaction **c**, with a bifurcation to two main reaction channels at the first step, itself mediated by relatively high barriers (**TS1_1d** and **TS1_5d**; ΔG_{rel} = 37.1 and 32.5 kcal·mol^{-1}, respectively). Apart from this "forking" and the subsequent insertion of the second alkyne equivalent serving as the RDS, the similarities to reaction **c** end there (**d** in Figure 3). Overall, the entire profile is much higher in energy, with the next lowest barrier being 60.4 kcal·mol^{-1}, for the second alkyne insertion along the **2d** pathway. All **INT2** → **INT3** isomerizations show much lower free energy barriers (ΔG_{rel} = 6.8−16.9 kcal·mol^{-1}) than **TS2** (**1d** to **8d** respectively). The elimination of product and concurrent catalyst regeneration

DOI: 10.1021/acs.joc.5b01464
J. Org. Chem. 2015, 80, 9108−9117

Table 1. Calculated Free Energy Barriers (ΔG_{rel}TS2, 363 K, kcal·mol^{-1}), Rate Constants (k, L·mol^{-1}·s^{-1}), Reaction Half-Life ($t_{1/2}$, h),[a] and End-Product Identity for All Reaction Channels and Pathways (1−8) of Reactions a−d, Determined at the IDSCRF-B3LYP/DGDZVP Level in THF Solvent, Together with the Corresponding Experimental Product Yields (%)

reaction channel	ΔG_{rel}TS2 (kcal·mol^{-1})	k (L·mol^{-1}·s^{-1})	$t_{1/2}$ (h)	compt products	exp. product (yield %)
1a	**27.2**	**3.183×10^{-4}**	**8.727×10^{-1}**	**P1a**	**P1a(67)**
2a	49.8	7.877×10^{-18}	3.526×10^{13}	P1a	
1b	**36.6**	**6.974×10^{-10}**	**3.983×10^{5}**	**P1b**	**P1b(33)**
2b	49.8	7.877×10^{-18}	3.526×10^{13}	P1b	
1c	**31.1**	**1.428×10^{-6}**	**1.945×10^{2}**	**P1c**	**P1c(54)**
2c	44.7	9.265×10^{-15}	2.998×10^{10}	P1c	
5c	46.2	1.158×10^{-15}	2.398×10^{11}	P1c	
6c	39.9	7.190×10^{-12}	3.863×10^{7}	P1c	
3c	52.6	1.624×10^{-19}	1.710×10^{15}	P2c	
4c	45.7	2.316×10^{-15}	1.199×10^{11}	P2c	
7c	43.3	6.453×10^{-14}	4.305×10^{9}	P3c	
8c	40.0	6.259×10^{-12}	4.438×10^{7}	P3c	
1d	84.3	1.335×10^{-38}	2.081×10^{34}	P1d	
2d	**60.4**	**3.270×10^{-24}**	**8.494×10^{19}**	**P1d**	**NR**
5d	78.0	8.288×10^{-35}	3.352×10^{30}	P1d	
6d	71.7	5.145×10^{-31}	5.399×10^{26}	P1d	
3d	79.8	6.835×10^{-36}	4.064×10^{31}	P2d	
4d	69.3	1.433×10^{-29}	1.938×10^{25}	P2d	
7d	82.7	1.227×10^{-37}	2.264×10^{33}	P3d	
8d	66.2	1.054×10^{-27}	2.636×10^{23}	P3d	

[a] $t_{1/2}$ is calculated from the half-life equation of second-order reaction, $t_{1/2} = (ka)^{-1}$, where a represents the initial concentration, with 1.0 mol·L^{-1} set as default.

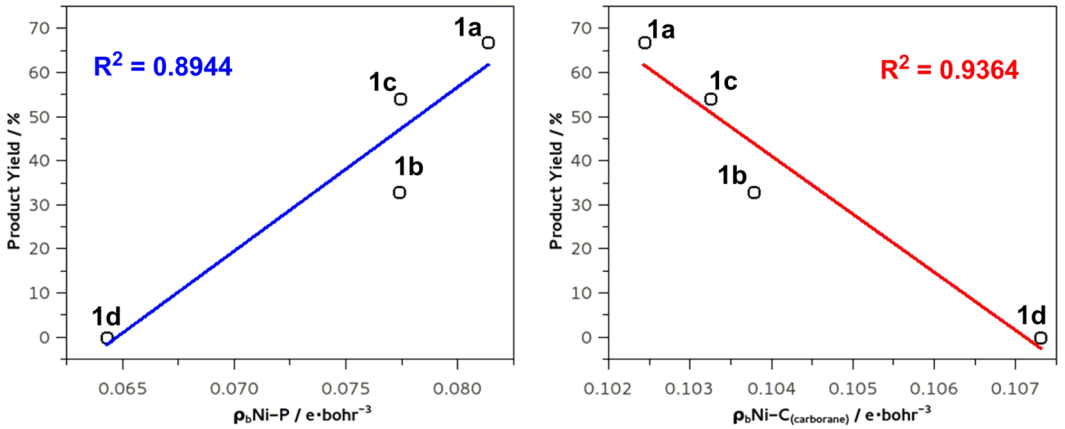

Figure 4. Plots of product yield (%) and electronic density (e·bohr^{-3}) in the Ni−P and Ni−C (carborane) bonds for the rate-determining **TS2** structure in reactions **a**−**d**. Yield rises with increased density in the Ni−P bond, while the inverse trend is observed for the Ni−C (carborane) one.

proceeds with relative overall ease (with respect to **TS2** barriers), displaying large variance in barrier energetics (ΔG_{rel} = 0.8−30.2 kcal·mol^{-1}) (Figure S2).

The barriers for the rate-determining second step along all eight pathways encompassing reaction **d** are >60 kcal·mol^{-1}.These unmanageable barriers are in agreement with the experimental observations of 0% yield for any of the products (**P1d**, **P2d**, and **P3d**, Scheme 1). Structural investigation shows dominating steric repulsions between the ^{t}Bu, ^{n}Bu, carboryne, and PPh_3 groups, with the latter two groups adjacent to one another, particularly in the **TS2_1d**, **TS2_3d**, **TS2_5d**, and **TS2_7d** structures (Figure S3). Correspondingly, these four structures have the highest relative **TS2** barriers of reaction **d** (ΔG_{rel} = 84.3, 79.8, 78.0, and 82.7 kcal·mol^{-1}, respectively).

2.3. Kinetics. Transition-state theory[13] provides an effective route to theoretically predicting related kinetics of such chemical transformations. The free energy barrier of the RDS quantitatively discloses reaction rate constants (k) and half-lives ($t_{1/2}$), providing a metric of the time-dependence of the observed regioselectivities (Table 1).

Avoiding explicitly revisiting the energetic trends already disseminated in the profiles within Figure 3, the kinetic results listed in Table 1 provide support for the experimentally determined products, specifically, the time-dependent reasoning for why channel **1a** dominates over **2a**, **1b** over **2b**, and **1c** over **2c**−**8c** and why, despite the domination of **2d** (over **1d** and **3d**−**8d**), no product is observed in reaction **d** where the reaction half-life for this "optimal" pathway (8.494×10^{19} h) is longer than the estimated age of the universe!

With respect to the experimental determinations (96 h for completion, and assuming $t_{1/2} \sim 48$ h in the absence of empirical values), the $t_{1/2}$ predictions are within 2 orders of magnitude for pathway **1a** (8.727×10^{-1} h ≈ 1 h) and 1 order of magnitude for **1c** (1.945×10^{2} h ≈ 200 h). Although the

DOI: 10.1021/acs.joc.5b01464
J. Org. Chem. 2015, 80, 9108−9117

Table 2. Experimental Yields (%) and Computed Relative Free Energies (ΔG_{rel}, kcal·mol^{-1}) of TS1 and TS2 on Optimal Pathways of Reactions a, b, c, and d (1a, 1b, 1c, and 2d, Respectively) Determined with the B3LYP, X3LYP, CAM-B3LYP, B3LYP+D3, and M062X Methods (All with DGDZVP Basis Set)[a]

		Method									
	Experimental	B3LYP		X3LYP		CAM-B3LYP		B3LYP+D3		M06-2X	
Reaction	Yield	TS1	TS2	TS1	TS2	TS1	TS2	TS1	TS2	TS1	TS2
a	67%	23.7	27.2	22.8	24.9	24.6	21.9	32.9	8.6	23.7	8.0
b	33%	26.8	36.6	24.3	34.6	28.8	34.2	31.7	8.2	24.7	15.6
c	54%	25.1	31.1	22.4	28.1	26.9	26.9	31.1	7.3	26.1	17.8
d	0%	37.1	60.4	36.6	56.9	38.7	56.6	42.6	32.6	36.9	39.0
$Yield_{Rel}$	a > c > b >> d	a > c > b >> d		a > c > b >> d		a > c > b >> d		c > b > a > d		a > b > c > d	

[a]The rate-determining step (RDS) for each method is highlighted in blue. Yield ordering are summarized for each method; for theory, based on relative barrier heights of RDSs. Theory-ordered yields not in agreement with experimental ordering are distinguished by red text.

Table 3. Calculated Free Energy Barriers of RDS (ΔG_{rel}, kcal·mol^{-1}), Rate Constants (k, L·mol^{-1}·s^{-1}), and Reaction Half-Life ($t_{1/2}$, h) for Optimal Reaction Channels of Reaction a, Determined Using the IDSCRF-B3LYP, IDSCRF-CAM-B3LYP, IDSCRF-B3LYP+D3, IDSCRF-M062X, and IDSCRF-X3LYP Methods in THF Solvent, Each Employing the DGDZVP Basis Set at 363 K[a]

method	ΔG_{rel}RDS (kcal·mol^{-1})	k (L·mol^{-1}·s^{-1})	$t_{1/2}$ (h)	Exp. $t_{1/2}$[d] (h)	deviation[e]
B3LYP	**27.2**[b]	**3.183 × 10^{-4}**	**8.727 × 10^{-1}**	**48**	**~50× faster**
X3LYP	24.9[b]	7.719 × 10^{-3}	3.599 × 10^{-2}	48	~1330× faster
CAM-B3LYP	24.6[c]	1.170 × 10^{-2}	2.374 × 10^{-2}	48	~2020× faster
B3LYP+D3	32.9[c]	1.178 × 10^{-7}	2.358 × 10^{3}	48	~50× slower
M062X	23.7[c]	4.074 × 10^{-2}	6.819 × 10^{-3}	48	~7030× faster

[a]Deviations of computed $t_{1/2}$ values from experimental ones are approximated. [b]**TS2_1a** = RDS. [c]**TS1_1a** = RDS. [d]Assuming experimental $t_{1/2} \approx 48$ h. [e]Theory relative to experiment.

results for **1b** are "off" by 3 orders of magnitude (3.983×10^5 h $\approx 4 \times 10^5$ h), they are within ±3.0 kcal·mol^{-1}. Overall, these results are quantitative with respect to experiment, as the accuracy required to be within 1 or 2 orders of magnitude (in hours for $t_{1/2}$) is ±0.75 and ±1.5 kcal·mol^{-1}, respectively. Thus, RDS free energy barrier predictions for reactions **a** and **c** approach and satisfy, respectively, the gold standard of current computational methods (1.0 kcal·mol^{-1}),[14] while those for reaction **b** are reasonable.

2.4. Trends across Reactions. With respect to potential reactivity trends across reactions **a**–**d**, analyses of the molecular graphs of the RDS (**TS2**) were plotted (Figure S4) and key interactions analyzed. The magnitude of electronic density in the catalyst metal–ligand bond (Ni–P) and metal–carboryne link (Ni–C) both show correlation with product yields across reactions **a**–**d** (Figure 4). In the former, the strengthening of the Ni–P link correlates with increased yields, attributed to the stabilizing of the catalyst at the RDS as well as for its potential regeneration. Strengthening of the Ni–C (carborane) bond at the RDS-TS results in product yield reduction, in this case attributed to bringing the Ni-coordination sphere detrimentally close to the bulky corborane moiety. This latter bond is very sensitive to modulation, where the ~4.5% increase in electronic density in the bond on moving from **TS2_1a** to **TS2_1d** (0.1024 → 0.1073) sends product yields tumbling from 67 to 0%.

Other interactions within the **TS2** structure did not show such statistical agreement, with quite poor R^2 values, as follows: Ni–C(rct2), R^2 = 0.7192; (rct1)C–C(rct2), R^2 = 0.7344; (rct1)C–C(carborane), R^2 = 0.6088; (carborane)C–C-(carborane), R^2 = 0.3900. The lack of a trend emerging for these bonds with respect to product yield across reactions **a**–**d** is attributed to the complex set of weakly polar interactions surrounding these atoms, as evidenced from the molecular graphs of their wave functions (Figure S4). Therein, at least one atom in three of the four pairs is part of one of the transiently bound reactants. The fourth, involving the carborane C–C bridge, shows no correlation at all.

2.5. Influence of Theoretical Method. Although free energy values from the B3LYP method are reasonable at the experimental temperature (363 K) and correspondingly ordered with experimental product yields 67%, 33%, 54%, and 0% for reactions **a**, **b**, **c**, and **d**, respectively, we have trialed other methods to further evolve the determinations. We exhaustively re-evaluated the optimal pathways of reactions **a**, **b**, **c**, and **d** employing the following four additional methods: CAM-B3LYP, B3LYP+D3, X3LYP, and M062X. Results are comparatively listed in Table 2 and 3, while detailed reaction profiles are presented in Figure S5–8.

The B3LYP and B3LYP-D3 methods make half-life predictions that are closest to the respective experimental values (Table 3). However, with respect to product yield the B3LYP-D3 method shows larger deviations than does B3LYP (Table 2). Overall, the results from the B3LYP method provide the closest match to experimental trends, including $t_{1/2}$ values (perhaps due to a "fortuitous cancellation of errors"!); thus, only these results are presented in full detail throughout this work.

2.6. Real vs Truncated Models. As a final curiosity and toward addressing the question of the reliability of truncated

DOI: 10.1021/acs.joc.5b01464
J. Org. Chem. 2015, 80, 9108–9117

Table 4. Calculated Free Energy Barriers (ΔG_{rel}, 363 K, kcal·mol^{-1}), Rate Constants (k, L·mol^{-1}·s^{-1}), and Reaction Half-Life ($t_{1/2}$, h) for the Optimal Reaction Channels of Reactions a−d, Determined at the IDSCRF-B3LYP/DGDZVP Level in THF Solvent, Together with Corresponding Experimental Product Yields (%) (363 K over 96 h)

Path	ΔG_{rel} (kcal•mol^{-1})[a]				k for RDS (L•mol^{-1}•s^{-1})	$t_{1/2}$ for RDS(h)	Yield(%)
	TS1	TS2	TS3	TS4			
1a	23.7	**27.2**	0.9	10.6	3.183×10^{-4}	8.727×10^{-1}	67
1am	**35.0**	20.8	6.3	11.2	6.409×10^{-9}	4.334×10^{4}	--
1am2	**31.1**	16.5	7.7	10.1	1.428×10^{-6}	1.945×10^{2}	--
$\Delta_{1a\text{-}1am}$	*-11.3*	*+6.4*	*-5.4*	*-0.6*			
$\Delta_{1a\text{-}1am2}$	*-7.4*	*+10.7*	*-6.8*	*+0.5*			
1b	26.8	**36.6**	6.8	13.3	6.974×10^{-10}	3.983×10^{5}	33
1bm	**34.9**	27.0	6.7	13.7	7.362×10^{-9}	3.773×10^{4}	--
1bm2	**32.6**	23.7	11.5	12.1	1.785×10^{-7}	1.556×10^{3}	--
$\Delta_{1b\text{-}1bm}$	*-8.1*	*+9.6*	*+0.1*	*-0.4*			
$\Delta_{1b\text{-}1bm2}$	*-5.8*	*+12.9*	*-4.7*	*+1.2*			
1c	25.1	**31.1**	4.9	13.0	1.428×10^{-6}	1.945×10^{2}	54
1cm	**32.8**	23.6	4.8	11.2	1.353×10^{-7}	2.053×10^{3}	--
1cm2	**31.4**	20.7	7.0	10.2	9.423×10^{-6}	2.948×10^{2}	--
$\Delta_{1c\text{-}1cm}$	*-7.7*	*+7.5*	*+0.1*	*+1.8*			
$\Delta_{1c\text{-}1cm2}$	*-6.3*	*+10.4*	*-2.1*	*+2.8*			
2d*	37.1	**60.4**	16.9	15.6	3.270×10^{-24}	8.494×10^{19}	NR
2dm*	49.3	**56.2**	14.6	6.2	1.105×10^{-21}	2.515×10^{17}	--
2dm2*	45.2	**52.0**	19.1	4.4	3.731×10^{-19}	7.445×10^{14}	--
$\Delta_{2d\text{-}2dm}$	*-12.2*	*+4.2*	+2.3	+9.4			
$\Delta_{2d\text{-}2dm2}$	*-8.1*	*+8.4*	*-2.2*	*+11.2*			

[a]The highest barriers (and thus RDSs) for each pathway are indicated in bold blue font.

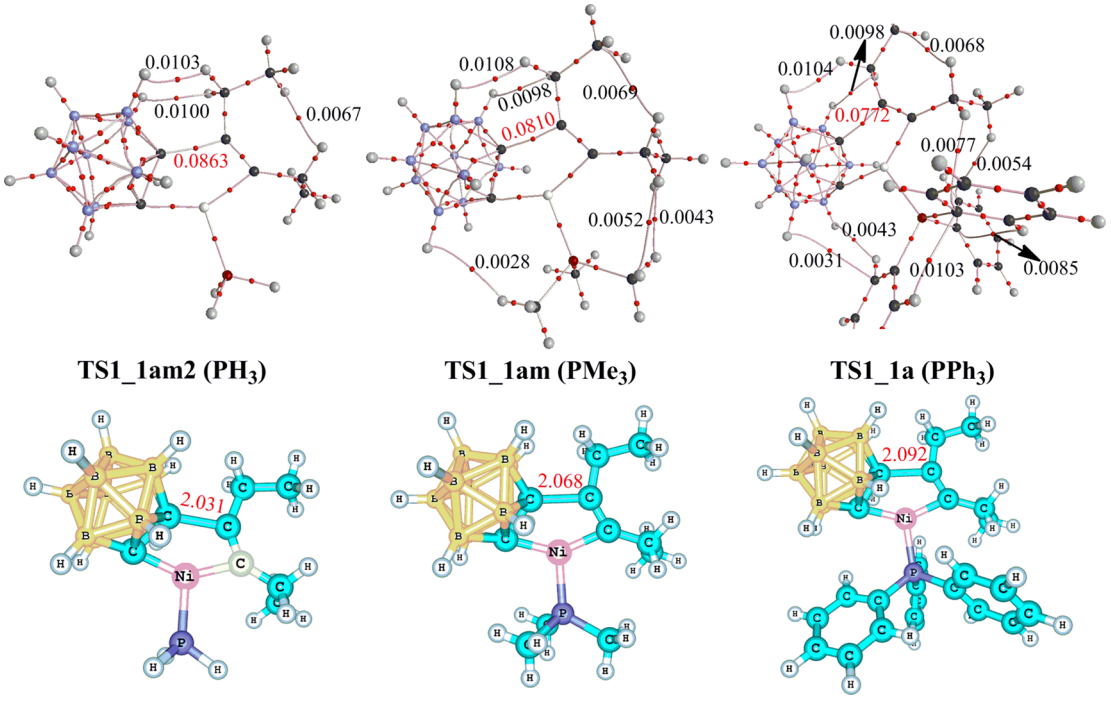

Figure 5. Molecular graphs of the wave functions (top) and structures (bottom) of the IDSCRF-B3LYP/DGDZVP geometry-optimized **TS1_1am2**, **TS1_1am**, and **TS1_1a**. Bond critical points (BCPs) are shown in red. For clarity, all ring critical points (RCPs) and cage critical points (CCPs) are omitted. Key bond lengths are shown in angstroms.

models, we recomputed the optimal channels in reactions **a**−**d** using PMe_3 (labeled **m**) and PH_3 (labeled **m2**) in place of the larger and computationally demanding PPh_3 ligand groups in the real catalyst system. Often, it is proposed that the coordination sphere of the catalytic metal provides the dominant contributions to reaction energetics and specificities, and thus, the extraneous atoms on ligand and reactant groups can be pruned to smaller model groups. Our results indicate otherwise, wherein the role of sterics and other such "secondary" forces do play dominating roles in the specificities of chemical transformations and regioselectivity.

The energetics trends for the truncated reactions **a**−**d** (labeled **am**−**dm** and **am2**−**dm2**, for reactions **a**−**d**, respectively) are comparatively summarized in Table 4. Detailed mechanisms and reaction profiles are presented in Figure S9 and the structures in Figures S10−S13 accordingly.

DOI: 10.1021/acs.joc.5b01464
J. Org. Chem. 2015, 80, 9108−9117

In all truncated profiles, the products arising from the PMe_3 truncated pathways (**P1am**, **P1bm**, **P1cm**, and **P1dm**) are all 16.2 kcal·mol^{-1} higher in free energy than their corresponding nontruncated products (**P1a**, **P1b**, **P1c**, and **P1d**, respectively). The RDS for reactions **am**−**cm** is **TS1** (1st insertion of alkyne), differing from the results for the full systems that show the insertion of the second equivalent (**TS2**) as having the highest, and thus kinetically controlling, barrier; reaction **dm** follows this trend (Table 4). All **TS1** free energy barriers for the PMe_3-truncated profiles are higher (by 7.7−12.2 kcal·mol^{-1}) than their corresponding free energy barriers in the real systems (nontruncated), due to the significant reduction of electron-withdrawing power of the Me and H groups on the phosphine, limiting the activation of the Et group during the first addition. Conversely, all **TS2** barriers are correspondingly lower (Table 4). For **TS3** (isomerization) and **TS4** (product elimination and concurrent regeneration of catalyst), no tractable reordering of barriers is observed, with changes ranging between −5.4 to +2.3 and −0.6 to +9.4 kcal·mol^{-1}, respectively. The topologies of all PMe_3 and PH_3-truncated pathways (**1am**, **1bm**, **1cm**, **2dm**, **1am2**, **1bm2**, **1cm2**, and **2dm2**) show similar trends; hence, the significant easing of the **TS2** free energy barriers with respect to the real PPh_3-ligated systems are a result of the reduction in sterics for the smaller ligand and the incoming/outgoing reactants.

Further comparison of molecular graphs of the wave functions generated from the geometry-optimized structures of **TS1_1am2**, **TS1_1am**, and **TS1_1a** are presented in Figure 5. Interactions between the carboryne and the PH_3 group or between PH_3 and the Et group were not located in the **TS1_1am2** structure (truncated to PH_3), while one BCP (0.0028 $\bar{e}$·bohr^{-3}) and two BCPs (0.0052 and 0.0043 $\bar{e}$·bohr^{-3}, respectively) were found in the **TS1_1am** structure (PMe_3-truncated), for the $_{[PMe3]}C-H\cdots H-B_{[carborane]}$ and $_{[PMe3]}C-H\cdots H-C_{[ethyl]}$. These interactions are indicative of the sterics between the PMe_3 groups and the carborane and Et groups. Dominating weak interactions are found in **TS1_1a** (real system, PPh_3), including two interactions linking the three Ph-groups (0.0103 and 0.0085 $\bar{e}$·bohr^{-3}, respectively), further supporting the importance of involving PPh_3 groups in modulation.

These results indicated that truncated models cannot accurately predict either the enthalpy or the entropy in such reactions since they are devoid of secondary interactions or effects not directly adjacent to the reaction center, including sterics or weakly polar interactions (i.e., van der Waals). The results presented in this work indicate that the real chemical systems should be employed in any characterizations of such Ni (or any other transition metal)-based catalyzed transformations. Likewise, to ensure accuracy in "computational steering" of synthetic enterprises seeking to optimize existing processes, or in the design of novel protocols, such undertakings must employ the full chemical systems.

3. CONCLUSIONS

Density functional theory (DFT) calculations at the IDSCRF-B3LYP/DGDZVP level at 363 K in THF solvent were carried out to investigate the reaction mechanisms, origins of substituent effect, and regioselectivities of $Ni(PPh_3)_2Cl_2$-catalyzed [2 + 2 + 2] cyclizations between carboryne and substituted alkynes for the first time. The results uncovered lead to the following conclusions:

(1) For all reactions characterized (reactions **a**−**d**), the second insertion of alkyne (via **TS2**) serves as the rate-determining step (RDS) in the formation of product (**P1a**, **P1b**, **P1c**, **P2c**, **P3c**, **P1d**, **P2d**, and **P3d**). For reactions **a**−**c**, this event is mediated by barriers of 27.2−36.6 kcal·mol^{-1}, respectively, surmountable under the experimental conditions (363 K in THF solvent) and in agreement with yielding of product. Further, the much higher barrier for reaction **d** (60.4 kcal·mol^{-1}) is in agreement with experimental determinations showing none of the **P1d**, **P2d**, and **P3d** products being generated.

(2) Theoretical predictions of kinetics aspects of the reactions rate constants (k) and half-lives ($t_{1/2}$) from the free energy barriers of the RDS show excellent agreement with experimental times and product yield distributions of regioisomers. The exponential nature of these kinetic variables and, thus, requisite accuracy of the theoretically determined free energy barriers (to within ∼ ± 0.75 kcal·mol^{-1}) evidence the theoretical results as being representative of the real world chemical transformations. The high RDS barriers (>60.0 kcal·mol^{-1}) of reaction **d** transform to overly long $t_{1/2}$ predictions and, thus, a prediction that the reaction would not proceed at the experimental temperature of 363 K, in agreement with experiment, showing no products being yielded. The overly bulky nature of the subsitutents is the logical empirical explanation, affirmed by examination of the geometry-optimized structures along the pathways of reaction **d**.

(3) The true chemical systems other than truncated or simplified models should be used in order to resolve accurate reproduction of energetic and kinetic aspects of the reactions. Herein, both substituents on the reactant alkynes and the central Ni-catalyst are crucial for accurate prediction of the free energy barriers. Comparative models using the full PPh_3 ligands and truncated PMe_3, PH_3 groups were used to evidence this, with the latter showing the first insertion of alkyne to be the RDS for reactions **a**-**c**, while predicting much lower barriers for the second insertion of alkyne (via **TS2**, lower by 4.2−9.6 and 8.4−12.9 kcal·mol^{-1}, respectively).

4. COMPUTATIONAL DETAILS

All stationary points were optimized and structures verified (as being chemically logical) using the Becke-3−Lee−Yang−Parr (B3LYP) method[15] as implemented in the Gaussian 09 Program Package (G09),[16] employing the standard double-ζ valence polarized (DGDZVP) all-electron basis set for all atoms;[17] except where noted elsewhere. The self-consistent reaction field (SCRF) polarizable continuum model (PCM)[18] was used to address solvent effects of THF (ε = 7.58, at 298.15 K), employing our recently established IDSCRF radii,[19] denoted IDSCRF-B3LYP, for geometry optimization and determinations. All optimized stationary points were subsequently characterized by frequency analyses using the same method/level to ensure that the structures found reside at minima and first-order saddle points, respectively, on their potential energy hypersurfaces. All free energies reported are calculated from standard determinations emerging from the G09 output. Solution-phase translational entropy contributions to free energy were employed.[20]

Toward resolving the influence of basis set and solvent on the results, comparative calculations about the optimal reaction channel (**1cm2**) of PH_3 truncated reaction **c** were carried out at the B3LYP/BS1 level in the gas phase, as well as at the IDSCRF-B3LYP/BS1 and IDSCRF-B3LYP/BS2 levels in THF solution; results are summarized in Figure S14. Therein, BS1 and BS2 refer to mixed basis sets employing the 6-31G(d,p) and 6-311++G(d,p) Pople basis sets,[21,22] respectively, for C, H, B, and P atoms, while the DGDZVP basis set is utilized for Ni in both cases.

DOI: 10.1021/acs.joc.5b01464
J. Org. Chem. 2015, 80, 9108−9117

Comparative analyses of relative ΔG values obtained directly from G09 at the B3LYP/BS1, IDSCRF-B3LYP/BS1(THF), IDSCRF-B3LYP/BS2(THF), and IDSCRF-B3LYP/DGDZVP(THF) levels (Figure S14 (a)) reveals the B3LYP/BS1 gas phase results are all lower than the other three levels. Considering the real chemical transformation proceeds in THF solvent, the gas-phase results are deemed nonrepresentative and thus unreliable; thus, they are not discussed in the main text.

Further comparison between ΔG_{rel} values (with solution-phase translational entropy contributions to free energy considered) shows the relative activation free energies obtained at IDSCRF-B3LYP/BS2 and IDSCRF-B3LYP/DGDZVP levels are in close agreement ((b) in Figure S14 (b)), while those obtained at the IDSCRF-B3LYP/BS1 level are all higher (with the exception of the **INT2_1cm2** → **TS3_1cm2** isomerization). With respect to the quantitative agreement and much more expensive computational costs of the IDSCRF-B3LYP/BS2 level with respect to those of IDSCRF-B3LYP/DGDZVP, all free energies reported in this work (except those in Figure S14) are based on results obtained at the IDSCRF-B3LYP/DGDZVP level.

All structures residing at stationary points identified were subsequently characterized by frequency analyses, from which their (relative) free energies were obtained, in addition to verifying the stationary points to be minima or first-order saddle points on the potential energy surface. Intrinsic reaction coordinate (IRC)[23] calculations with the Hessian-based predictor−corrector integrator (HPC) were also used to confirm selected transition-state structures as connecting the two adjacent minima on their respective potential energy hypersurfaces.

The electronic structures of selected structures were analyzed by Bader's QTAIM theory[24] to quantitatively characterize the topological properties of the electron density distributions. Analyses were carried out on the wave functions generated using the IDSCRF-B3LYP/DGDZVP method on the geometry-optimized structures. All molecular graphs of wave functions reported in this manuscript have been performed with the AIM2000 program package.[25]

■ ASSOCIATED CONTENT

Supporting Information

The Supporting Information is available free of charge on the ACS Publications website at DOI: 10.1021/acs.joc.5b01464.

Optimized Cartesian coordinates for all stationary points; vibrational frequencies; total energies, zero-point energies and total free energies; complementary mechanistic characterizations (PDF)

■ AUTHOR INFORMATION

Corresponding Authors

*E-mail: weihua_mu@ynnu.edu.cn.
*E-mail: g.chass@qmul.ac.uk.

Notes

The authors declare no competing financial interest.

■ ACKNOWLEDGMENTS

This work was supported by the National Natural Science Foundation of China (21363028, 21373030) and the Chunhui Project of Ministry of Education of the PRC (Z2009-1-65003). G.A.C. thanks the Science and Technology Facilities Council (STFC, UK) and the Royal Society of Chemistry, UK, for generous support. G.A.C. and D.C.F. thank the Royal Society of Chemistry, UK (project IE120096), and GIOCOMMS (Toronto/Budapest/Beijing) for supporting international research exchanges. G.A.C. acknowledges the support of the EPSRC, UK (projects EP/H030077/1, EP/H030077/2). and STFC, UK, for generous support.

■ REFERENCES

(1) (a) Medina, S.; Domínguez, G.; Pérez-Castells, J. *Org. Lett.* **2012**, *14*, 4982. (b) Rajeshkumar, V.; Lee, T.-H.; Chuang, S.-C. *Org. Lett.* **2013**, *15*, 1468. (c) Li, G.; Qian, S.; Wang, C.; You, J. *Angew. Chem., Int. Ed.* **2013**, *52*, 7837. (d) Araki, T.; Noguchi, K.; Tanaka, K. *Angew. Chem., Int. Ed.* **2013**, *52*, 5617. (e) Kuram, M. R.; Bhanuchandra, M.; Sahoo, A. K. *Angew. Chem., Int. Ed.* **2013**, *52*, 4607. (f) Lennox, A. J. J.; Lloyd-Jones, G. C. *Chem. Soc. Rev.* **2014**, *43*, 412. (g) Chen, W.; Fu, X.; Lin, L.; Yuan, X.; Luo, W.; Feng, J.; Liu, X.; Feng, X. *Chem. Commun.* **2014**, *50*, 11480. (h) Leckie, S. M.; Harkness, G. J.; Clarke, M. L. *Chem. Commun.* **2014**, *50*, 11511. (i) Mao, Z.; Huang, F.; Yu, H.; Chen, J.; Yu, Z.; Xu, Z. *Chem. - Eur. J.* **2014**, *20*, 3439. (j) Tan, F.; Lu, L.-Q.; Yang, Q.-Q.; Guo, W.; Bian, Q.; Chen, J.-R.; Xiao, W.-J. *Chem. - Eur. J.* **2014**, *20*, 3415. (k) Wang, L.; He, W.; Yu, Z. *Chem. Soc. Rev.* **2013**, *42*, 599.

(2) (a) Ogoshi, S.; Nishimura, A.; Ohashi, M. *Org. Lett.* **2010**, *12*, 3450. (b) Miura, T.; Morimoto, M.; Murakami, M. *J. Am. Chem. Soc.* **2010**, *132*, 15836. (c) Stolley, R. M.; Maczka, M. T.; Louie, J. *Eur. J. Org. Chem.* **2011**, *2011*, 3815. (d) Noucti, N. N.; Alexanian, E. J. *Angew. Chem., Int. Ed.* **2013**, *52*, 8424. (e) Aillard, P.; Retailleau, P.; Voituriez, A.; Marinetti, A. *Chem. Commun.* **2014**, *50*, 2199. (f) Hoshimoto, Y.; Ohata, T.; Ohashi, M.; Ogoshi, S. *Chem. - Eur. J.* **2014**, *20*, 4105.

(3) Deng, L.; Chan, H.-S.; Xie, Z. *J. Am. Chem. Soc.* **2006**, *128*, 7728.

(4) (a) Gann, A. W.; Amoroso, J. W.; Einck, V. J.; Rice, W. P.; Chambers, J. J.; Schnarr, N. A. *Org. Lett.* **2014**, *16*, 2003. (b) Gao, J.; Jankiewicz, B. J.; Reece, J.; Sheng, H.; Cramer, C. J.; Nash, J. J.; Kenttämaa, H. I. *Chem. Sci.* **2014**, *5*, 2205. (c) Oliva-Madrid, M.; Saura-Llamas, I.; Bautista, D.; Vicente, J. *Chem. Commun.* **2013**, *49*, 7997. (d) Feltenberger, J. B.; Hayashi, R.; Tang, Y.; Babiash, E. S. C.; Hsung, R. P. *Org. Lett.* **2009**, *11*, 3666. (e) Berry, R. S.; Clardy, J.; Schafer, M. E. *J. Am. Chem. Soc.* **1964**, *86*, 2738. (f) Jones, M., Jr.; Levin, R. H. *J. Am. Chem. Soc.* **1969**, *91*, 6411. (g) Sander, W. *Acc. Chem. Res.* **1999**, *32*, 669. (h) Deaton, K. R.; Gin, M. S. *Org. Lett.* **2003**, *5*, 2477. (i) Wang, B.; Mu, B.; Chen, D.; Xu, S.; Zhou, X. *Organometallics* **2004**, *23*, 6225. (j) Hamura, T.; Ibusuki, Y.; Uekusa, H.; Matsumoto, T.; Suzuki, K. *J. Am. Chem. Soc.* **2006**, *128*, 3534. (k) Zeidan, T. A.; Manoharan, M.; Alabugin, I. V. *J. Org. Chem.* **2006**, *71*, 954. (l) Gann, A. W.; Amoroso, J. W.; Einck, V. J.; Rice, W. P.; Chambers, J. J.; Schnarr, N. A. *Org. Lett.* **2014**, *16*, 2003.

(5) (a) Qiu, Z.; Xie, Z. *Sci. China, Ser. B: Chem.* **2009**, *52*, 1544. (b) Qiu, Z.; Deng, L.; Xie, Z. *J. Organomet. Chem.* **2013**, *747*, 225.

(6) (a) Qiu, Z.; Xie, Z. *J. Am. Chem. Soc.* **2009**, *131*, 2084. (b) Qiu, Z.; Xie, Z. *J. Am. Chem. Soc.* **2010**, *132*, 16085. (c) Qiu, Z.; Wang, S. R.; Xie, Z. *Angew. Chem.* **2010**, *122*, 4753; *Angew. Chem., Int. Ed.* **2010**, *49*, 4649. (d) Qiu, Z.; Ren, S.; Xie, Z. *Acc. Chem. Res.* **2011**, *44*, 299. (e) Ren, S.; Qiu, Z.; Xie, Z. *J. Am. Chem. Soc.* **2012**, *134*, 3242. (f) Wang, S. R.; Xie, Z. *Tetrahedron* **2012**, *68*, 5269. (g) Ren, S.; Qiu, Z.; Xie, Z. *Organometallics* **2012**, *31*, 4435. (h) Ren, S.; Qiu, Z.; Xie, Z. *Angew. Chem., Int. Ed.* **2012**, *51*, 1010. (i) Quan, Y.; Zhang, J.; Xie, Z. *J. Am. Chem. Soc.* **2013**, *135*, 18742. (j) Quan, Y.; Qiu, Z.; Xie, Z. *J. Am. Chem. Soc.* **2014**, *136*, 7599.

(7) Wang, S. R.; Xie, Z. *Organometallics* **2012**, *31*, 3316.

(8) Wang, S. R.; Qiu, Z.; Xie, Z. *J. Am. Chem. Soc.* **2010**, *132*, 9988.

(9) Wang, S. R.; Qiu, Z.; Xie, Z. *J. Am. Chem. Soc.* **2011**, *133*, 5760.

(10) Wang, S. R.; Xie, Z. *Organometallics* **2012**, *31*, 4544.

(11) (a) Ren, S.; Qiu, Z.; Xie, Z. *Organometallics* **2013**, *32*, 4292. (b) Qiu, Z.; Xie, Z. *Dalton Trans.* **2014**, *43*, 4925.

(12) Zhang, J. J.; Quan, Y. J.; Lin, Z. Y.; Xie, Z. *Organometallics* **2014**, *33*, 3556.

(13) (a) Lin, S. H.; Lau, K. H.; Volk, L.; Richardson, W.; Eyring, H. *Proc. Natl. Acad. Sci. U. S. A.* **1972**, *69*, 2778. (b) Volk, L.; Richardson, W.; Lau, K. H.; Hall, M.; Lin, S. H. *J. Chem. Educ.* **1977**, *54*, 95.

(14) Armstrong, A.; Boto, R. A.; Dingwall, P.; Contreras-García, J.; Harvey, M. J.; Mason, N. J.; Rzepa, H. S. *Chem. Sci.* **2014**, *5*, 2057.

(15) (a) Lee, C.; Yang, W.; Parr, R. G. *Phys. Rev. B: Condens. Matter Mater. Phys.* **1988**, *37*, 785. (b) Becke, A. D. *J. Chem. Phys.* **1993**, *98*, 5648.

DOI: 10.1021/acs.joc.5b01464
J. Org. Chem. 2015, 80, 9108−9117

(16) Frisch, M. J.; Trucks, G. W.; Schlegel, H. B.; Scuseria, G. E.; Robb, M. A.; Cheeseman, J. R.; Scalmani, G.; Barone, V.; Mennucci, B.; Petersson, G. A.; Nakatsuji, H.; Caricato, M.; Li, X.; Hratchian, H. P.; Izmaylov, A. F.; Bloino, J.; Zheng, G.; Sonnenberg, J. L.; Hada, M.; Ehara, M.; Toyota, K.; Fukuda, R.; Hasegawa, J.; Ishida, M.; Nakajima, T.; Honda, Y.; Kitao, O.; Nakai, H.; Vreven, T.; Montgomery, J. A., Jr.; Peralta, J. E.; Ogliaro, F.; Bearpark, M.; Heyd, J. J.; Brothers, E.; Kudin, K. N.; Staroverov, V. N.; Keith, T.; Kobayashi, R.; Normand, J.; Raghavachari, K.; Rendell, A.; Burant, J. C.; Iyengar, S. S.; Tomasi, J.; Cossi, M.; Rega, N.; Millam, J. M.; Klene, M.; Knox, J. E.; Cross, J. B.; Bakken, V.; Adamo, C.; Jaramillo, J.; Gomperts, R.; Stratmann, R. E.; Yazyev, O.; Austin, A. J.; Cammi, R.; Pomelli, C.; Ochterski, J. W.; Martin, R. L.; Morokuma, K.; Zakrzewski, V. G.; Voth, G. A.; Salvador, P.; Dannenberg, J. J.; Dapprich, S.; Daniels, A. D.; Farkas, O.; Foresman, J. B.; Ortiz, J. V.; Cioslowski, J.; Fox,D. J. *Gaussian 09, Revision D.01*, Gaussian, Inc., Wallingford, CT, 2013.

(17) (a) Godbout, N.; Salahub, D. R.; Andzelm, J.; Wimmer, E. *Can. J. Chem.* **1992**, *70*, 560. (b) Sosa, C.; Andzelm, J.; Elkin, B. C.; Wimmer, E.; Dobbs, K. D.; Dixon, D. A. *J. Phys. Chem.* **1992**, *96*, 6630.

(18) (a) Miertus, S.; Scrocco, E.; Tomasi, J. *Chem. Phys.* **1981**, *55*, 117. (b) Scalmani, G.; Frisch, M. J. *J. Chem. Phys.* **2010**, *132*, 114110.

(19) (a) Tao, J.-Y.; Mu, W.-H.; Chass, G. A.; Tang, T.-H.; Fang, D.-C. *Int. J. Quantum Chem.* **2013**, *113*, 975. (b) Fang, D.-C. *SCRFRADII*; Beijing Normal University: Beijing, China, free of charge for academic users.

(20) Fang, D.-C. *THERMO*; Beijing Normal University, Beijing, China, free of charge for academic users.

(21) Scott, A. P.; Radom, L. *J. Phys. Chem.* **1996**, *100*, 16502.

(22) (a) McLean, A. D.; Chandler, G. S. *J. Chem. Phys.* **1980**, *72*, 5639. (b) Krishnan, R.; Binkley, J. S.; Seeger, R.; Pople, J. A. *J. Chem. Phys.* **1980**, *72*, 650.

(23) (a) Gonzalez, C.; Schlegel, H. B. *J. Chem. Phys.* **1989**, *90*, 2154. (b) Gonzalez, C.; Schlegel, H. B. *J. Phys. Chem.* **1990**, *94*, 5523.

(24) (a) Bader, R. F. W. *Chem. Rev.* **1991**, *91*, 893. (b) Bader, R. F. W. *Atoms in Molecules: A Quantum Theory*; Clarendon Press: Oxford, U.K., 1990.

(25) (a) Biegler-Konig, F.; Schonbohm, J.; Bayles, D. *J. Comput. Chem.* **2001**, *22*, 545. (b) Biegler-Konig, F.; Schonbohm, J. *J. Comput. Chem.* **2002**, *23*, 1489.

DOI: 10.1021/acs.joc.5b01464
J. Org. Chem. 2015, 80, 9108−9117